Iranian Journal of Pharmaceutical Sciences
2026: 22 (1): 451- 465
https://journals.sbmu.ac.ir/IJPS

Research Article

Computational Modeling Reveals Mechanisms of Iridoids from *Pterocephalus hookeri* as Potential Inhibitors of Hepatocellular Carcinoma

Hung Duc Nguyen*

Faculty of Biology, Thai Nguyen University of Education, 24000, Thai Nguyen, Vietnam.

Received: December 9, 2025 **Accepted:** October 10, 2026 **Available online:** November 4, 2026.

Abstract

Primary liver cancer remains a significant global health burden, ranking among the most frequently diagnosed malignancies and a leading cause of cancer-related death. Iridoids isolated from *Pterocephalus hookeri* have demonstrated anti-hepatocellular carcinoma activity; however, their molecular mechanisms, particularly those involving apoptosis regulators, remain unclear. Here, we evaluated iridoid-derived candidates from P. hookeri as potential inhibitors of the anti-apoptotic Bcl-2 protein (PDB: 6GL8) using an integrated *in silico* workflow comprising molecular docking, 100 ns molecular dynamics simulations, MMGBSA free-energy estimation, ADMET prediction, and DFT calculations. Docking identified CPD6 as the top-ranked ligand (-7.68 kcal/mol), outperforming Paclitaxel (-6.18 kcal/mol) and forming key hydrogen bonds with Gln118 and Arg129. MD simulations supported the stable binding of CPD6-6GL8, with persistent hydrogen-bond occupancy. MMGBSA yielded ΔTOTAL of -27.28 ± 4.80 kcal/mol for CPD6 versus -30.47 ± 7.30 kcal/mol for Paclitaxel, with CPD6 showing favorable gas-phase stabilization but a higher solvation penalty. ADMET suggested comparable solubility and no hepatotoxicity alert for CPD6, though with reduced predicted intestinal absorption. DFT descriptors further characterized CPD6's electronic properties. Overall, CPD6 is a promising Bcl-2 inhibitory scaffold for hepatocellular carcinoma and warrants optimization and experimental validation.

Keywords: Anti-apoptosis; Bcl-2; DFT; Iridoids; Molecular docking; *Pterocephalus hookeri.*

1. Introduction

Primary liver cancer was the sixth most frequently diagnosed malignancy worldwide in 2022. However, it ranked as the third leading cause of cancer-related mortality, with an estimated 865,000 new cases and 757,948 deaths, reflecting its aggressive clinical course and unfavorable prognosis [1]. Hepatocellular carcinoma, accounting for approximately 75-90% of primary liver cancers, arises from hepatocytes and typically presents as a solid hepatic mass with predominant trabecular, pseudoglandular/acinar, and compact/solid growth patterns [2]. The B-cell lymphoma 2 (Bcl-2) family of proteins includes key anti-apoptotic members often overexpressed in hepatocellular carcinoma, helping cancer cells survive, resist treatment, and promote tumor growth by blocking programmed cell death [3]. Bcl-2 is the original and founding member of the Bcl-2 family, an anti-apoptotic protein whose function was first understood through its involvement in the t(14;18) chromosomal translocation, a hallmark of

*** Corresponding Author**:
Hung Duc Nguyen, Faculty of Biology, Thai Nguyen University of Education, 24000, Thai Nguyen, Vietnam. E-mail: hungnd@tnue.edu.vn.

Cite this article as: Duc Nguyen H. Computational Modeling Reveals Mechanisms of Iridoids from *Pterocephalus hookeri* as Potential Inhibitors of Hepatocellular Carcinoma. Iran. J. Pharm. Sci., 2026, 22 (1): 451-465.

DOI: https://doi.org/10.22037/ijps.v22i1.51121

This open-access article is distributed under the terms of the Creative Commons Attribution Non Commercial 4.0 License (CC BY-NC 4.0).

follicular lymphoma that leads to overexpression and prevents cancer cells from dying [4]. This translocation places the Bcl-2 gene next to the immunoglobulin enhancer, causing high protein production that blocks programmed cell death and promotes cell survival, a key feature of many cancers [5]. Thus, blocking anti-apoptotic Bcl-2 proteins can restore natural cell death and overcome resistance to traditional chemotherapy and radiation in hepatocellular carcinoma.

Medicinal plants have been extensively investigated for anticancer potential and remain a major reservoir for discovering new therapeutic agents. Numerous plant-derived compounds have been reported to act through complementary mechanisms, including inducing programmed cell death, suppressing tumor growth and angiogenesis, and modulating [6]. Translating such bioactive scaffolds into clinically used medicines further supports the pharmacological relevance of natural-product-centered discovery pipelines. Consistent with this paradigm, approximately 40% of FDA-approved drugs are natural products, natural product derivatives, or synthetic agents inspired by natural product structures [7]. Among those compounds, iridoids, a class of plant-derived monoterpenoids that exhibit a broad spectrum of bioactivities, have garnered significant attention for applications in the pharmaceutical industry. Scientific studies indicate that natural iridoids exhibit promising anti-liver cancer potential through various mechanisms, including the inhibition of cancer cell proliferation, migration, and angiogenesis [8-10]. Given the promising anti-liver cancer potential of iridoids, attention has increasingly turned to iridoid-rich medicinal plants as plausible sources of hepatocellular carcinoma active constituents, including *Pterocephalus hookeri* (C.B. Clarke) Höeck. This species, known as "pang-zi-duo-wo" in traditional Tibetan medicine, has been used for thousands of years to clear heat, detoxify, dispel wind, and relieve pain [11]. A previous study on this species isolated several iridoids with anti-hepatocellular carcinoma activity against the Huh-7 cancer cell line [12].

Nevertheless, the molecular basis of their activity, particularly pathways involving key regulators of apoptosis, remains insufficiently clarified. Accordingly, we performed a comprehensive in silico investigation to elucidate the potential mechanisms of these iridoids using an integrated computational approach, including molecular docking, molecular dynamics simulations, MMGBSA free-energy calculations, ADMET profiling, and DFT analyses. Collectively, these results provide a rationale for downstream experimental confirmation and optimization of these compounds as prospective agents for hepatocellular carcinoma, with favorable safety profiles pending further *in vitro* and *in vivo* studies.

2. Materials and methods

2.1. Structural preparation of selected ligands

These selected iridoids, including ptehoside A (CPD1), ptehoside B (CPD2), ptehoside I (CPD3), 7-*epi*-vogeloside (CPD4), vogeloside (CPD5), sylvestroside IV (CPD6), sylvestroside IV dimethyl acetal (CPD7), have molecular formulas of $C_{18}H_{21}NO_5$, $C_{15}H_{24}O_8$, $C_{32}H_{45}NO_{15}$, $C_{18}H_{26}O_9$, $C_{18}H_{26}O_9$, $C_{27}H_{36}O_{14}$, $C_{27}H_{40}O_{13}$, respectively, with molecular weights of 331.1420, 332.1471, 683.2789, 386.1577, 386.1577, 584.2105, 572.2469 Da. Paclitaxel, possessing a molecular formula of $C_{47}H_{51}NO_{14}$ and a molecular weight of 853.3310 Da, was chosen as the positive control (**Figure 1**).

2.2. Molecular docking

The three-dimensional structures of the selected ligands were generated in PDB format using BioVIVA Discovery Studio Visualizer, in which polar hydrogens were added, Gasteiger charges were assigned, and torsional bonds were treated as flexible. We obtained the Bcl-2 protein structure (PDB ID: 6GL8) from the RCSB Protein Data Bank in PDB format [13]. Ligand-protein docking was performed using AutoDock Tools, with a grid box of 60 points along each of the x, y, and z axes, spaced 0.375 Å apart. The binding pocket of 6GL8 was defined by coordinates x = 9.866 Å, y = 0.590 Å, and z = 16.717 Å. We explored docking poses using the Lamarckian genetic algorithm, which helped identify the lowest-energy conformations and favored stable interaction profiles. After docking, the top-ranked pose for each ligand was analyzed in Discovery Studio Client 2024 and compared with the docking profile of Tamoxifen on the same protein to assess similarities in binding behavior [14].

This open-access article is distributed under the terms of the Creative Commons Attribution Non Commercial 4.0 License (CC BY-NC 4.0).

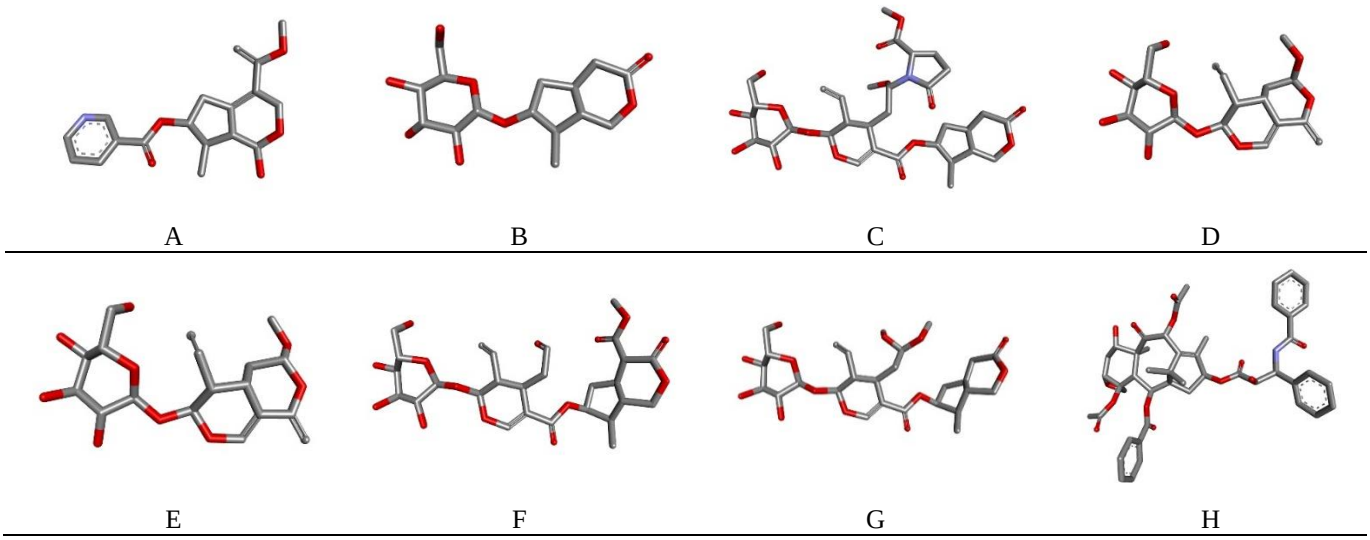


Figure 1. 3D Structures of selected ligands. (A) CPD1, (B) CPD2, (C) CPD3, (D) CPD4, (E) CPD5, (F) CPD6, (G) CPD7, (H) Paclitaxel.

2.3. Molecular dynamics simulation

We performed molecular dynamics simulations on the top-ranked docking pose of the ligand in complex with the Bcl-2 protein (PDB ID: 6GL8) for 100 ns using GROMACS 2024.4, with careful optimization of neighbor searching and inner-x [15]. Before simulation, we refined the protein structure in Swiss-PdbViewer by reconstructing missing residues and atoms [16]. We generated force-field parameters for the ligand with SwissParam [17]. The resulting complex was then placed in a triclinic water box employing the SPC model and supplemented with 0.15 M NaCl to mimic physiological ionic strength. We minimized the energy for 50,000 steps to relieve steric clashes and stabilize electrostatic interactions. System equilibration followed a two-stage protocol: a 200 ps NVT run followed by a 200 ps NPT phase, each maintained at 300 K and 1 bar. We performed production dynamics in triplicate, with each simulation extending 100 ns using a 2 fs timestep, and saved trajectory snapshots every 10 ns. We used Grace to quantify key dynamical descriptors, including root mean square deviation (RMSD), root mean square fluctuation (RMSF), radius of gyration (Rg), number of hydrogen bonds, and solvent-accessible surface area (SASA). Structural superimposition in UCSF Chimera 1.13.3 enabled evaluation of conformational stability across the simulated systems [18]. To examine interaction persistence, we aligned ligand orientations at the beginning (0 ns) and end (100 ns) of the simulation within the binding pocket. This comparison enabled assessment of the continuity of critical interactions, including hydrogen bonding, van der Waals contacts, and hydrophobic contributions, over the full 100 ns simulation, providing insights into the complex's durability and behavior throughout the simulation.

2.4. Molecular mechanics generalized born surface area (MMGBSA) analysis

Binding free energy calculations for the CPD6-6GL8 and Paclitaxel-6GL8 complexes were performed using the gmx_MMPBSA package together with the CHARMM36 force field. Polar contributions to the solvation energy were estimated using the generalized Born implicit solvent model, while non-polar components were determined from solvent-accessible surface area calculations. The analysis was based on molecular dynamics trajectories extracted over an 80 ns interval (20-100 ns), yielding 125 uniformly spaced frames at 80 ps intervals. This ensemble-based approach enabled a detailed comparison of interaction energetics between the two ligands, providing insight into their relative binding strengths and the stability of each complex throughout the simulation period [19].

This open-access article is distributed under the terms of the Creative Commons Attribution Non Commercial 4.0 License (CC BY-NC 4.0).

2.5. Assay protocol for ADMET prediction

Evaluating ADMET characteristics is a crucial step in identifying potential pharmacokinetic or safety concerns early in drug development, thereby minimizing late-stage attrition and increasing the likelihood of discovering compounds with suitable therapeutic profiles. In this study, the pkCSM platform was utilized to predict the ADMET properties of CPD6 and Paclitaxel. The tool uses graph-based molecular descriptors to generate predictions, enabling a systematic assessment of absorption, distribution, metabolism, excretion, and toxicity for the selected molecules.

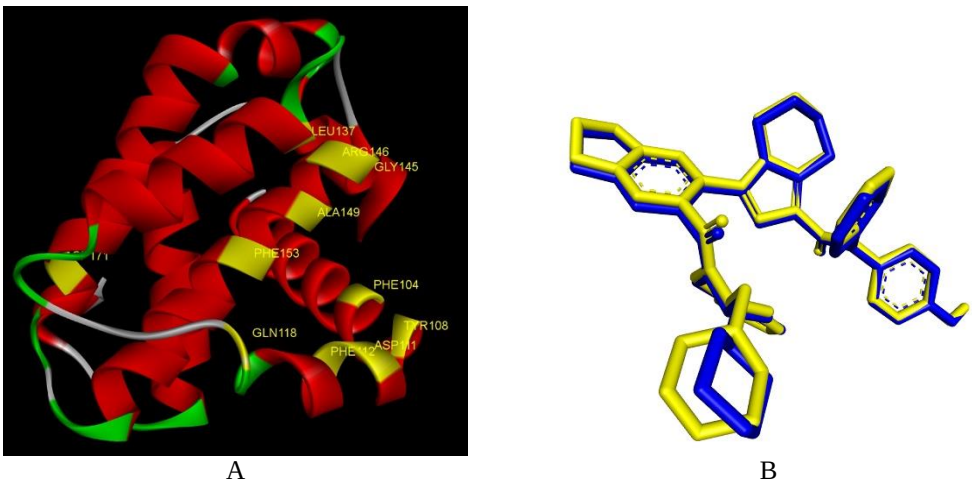
2.6. Quantum chemistry computation using the Density Functional Theory (DFT) method

We performed molecular geometry optimization for CPD6 and Paclitaxel using the ORCA quantum chemistry suite (version 6.1.0). We built initial structural models in Avogadro and performed molecular orbital visualization and related electronic analyses in IboView (version 20211019) [20-22]. All density functional theory calculations employed the B3LYP functional paired with the 6-31G(d,p) basis set to obtain reliable electronic wavefunctions. From the fully optimized geometries, a series of quantum-chemical descriptors were derived, including the energies of the highest occupied molecular orbital (HOMO) and the lowest unoccupied molecular orbital (LUMO), the HOMO-LUMO energy gap (ΔE), chemical potential (μ), electronegativity (χ), global hardness (η), softness (σ), and electrophilicity index (ω). These reactivity parameters were evaluated using Koopmans' theorem to characterize the electronic properties and chemical behavior of the compounds under study [23, 24].

3. Results and discussion

3.1. Molecular docking analysis

Molecular docking predicts a drug's binding site and interaction strength with a target protein, revealing how strongly it binds and its optimal orientation. This understanding helps elucidate the mechanism of action and potential therapeutic effects by showing specific molecular interactions, such as hydrogen bonds and hydrophobic contacts. This computational method identifies promising drug candidates by assessing binding energy and modeling the complex's geometry to predict drug-target engagement, a crucial step in drug discovery [25]. This investigation analyzed the binding affinities and intermolecular interactions between the 6GL8 protein and selected iridoids, using Paclitaxel as the reference compound. Structural assessment of the 6GL8 protein revealed active sites consisting of residues Phe104, Tyr108, Asp111, Phe112, Gln118, Leu137, Gly145, Arg146, Ala149, Phe153, and Asp171, as illustrated in **Figure 2A**. Before molecular docking, we validated the docking protocol by re-docking the crystallographic ligand of the 6GL8 protein. The reliability of the docking methodology was confirmed by an RMSD value of 0.4522 Å obtained from the superimposition of the native ligand conformation and the re-docked pose, as shown in **Figure 2B**. An RMSD value below 2 Å is indicative of a robust and dependable docking strategy.



A B

Figure 2. Active sites in the 6GL8 protein (A) and the superposition of the docked and original (B)

This open-access article is distributed under the terms of the Creative Commons Attribution Non Commercial 4.0 License (CC BY-NC 4.0).

As shown in **Table 1**, docking-derived affinities and non-covalent interaction profiles were compared for seven candidate ligands (CPD1-CPD7) against a shared binding pocket defined by recurrent residues such as Phe104, Tyr108, Asp111, Phe112, Gln118, Leu137, Ala149, and Phe153, using Paclitaxel as a reference compound. The interaction inventory encompassed hydrogen-bonding, van der Waals contacts, and hydrophobic interactions as annotated for each complex; taken together, these non-covalent forces support complex integrity by providing directional hydrogen-bond constraints that favor precise alignment with electronegative atoms, hydrophobic clustering that reduces solvent exposure and promotes compact packing, and short-range van der Waals complementarity that adds incremental stabilization and refines association energetics and kinetics [26, 27]. Across the series, binding energies spanned from -7.68 to -6.51 kcal/mol for CPD1-CPD7, while Paclitaxel displayed -6.18 kcal/mol, indicating weaker predicted stabilization than every CPD ligand under the same docking setup.

Among all ligands, CPD6 produced the most favorable affinity (-7.68 kcal/mol) and a dense contact network totaling 15 interactions, including 2 hydrogen bonds (Gln118, Arg129), 10 van der Waals contacts (Phe104, Asp111, Met115, Leu119, Thr132, Glu136, Leu137, Ala149, Glu152, Phe153), and 3 hydrophobic contacts (Tyr108, Phe112, Val133) (**Figure 3A**).

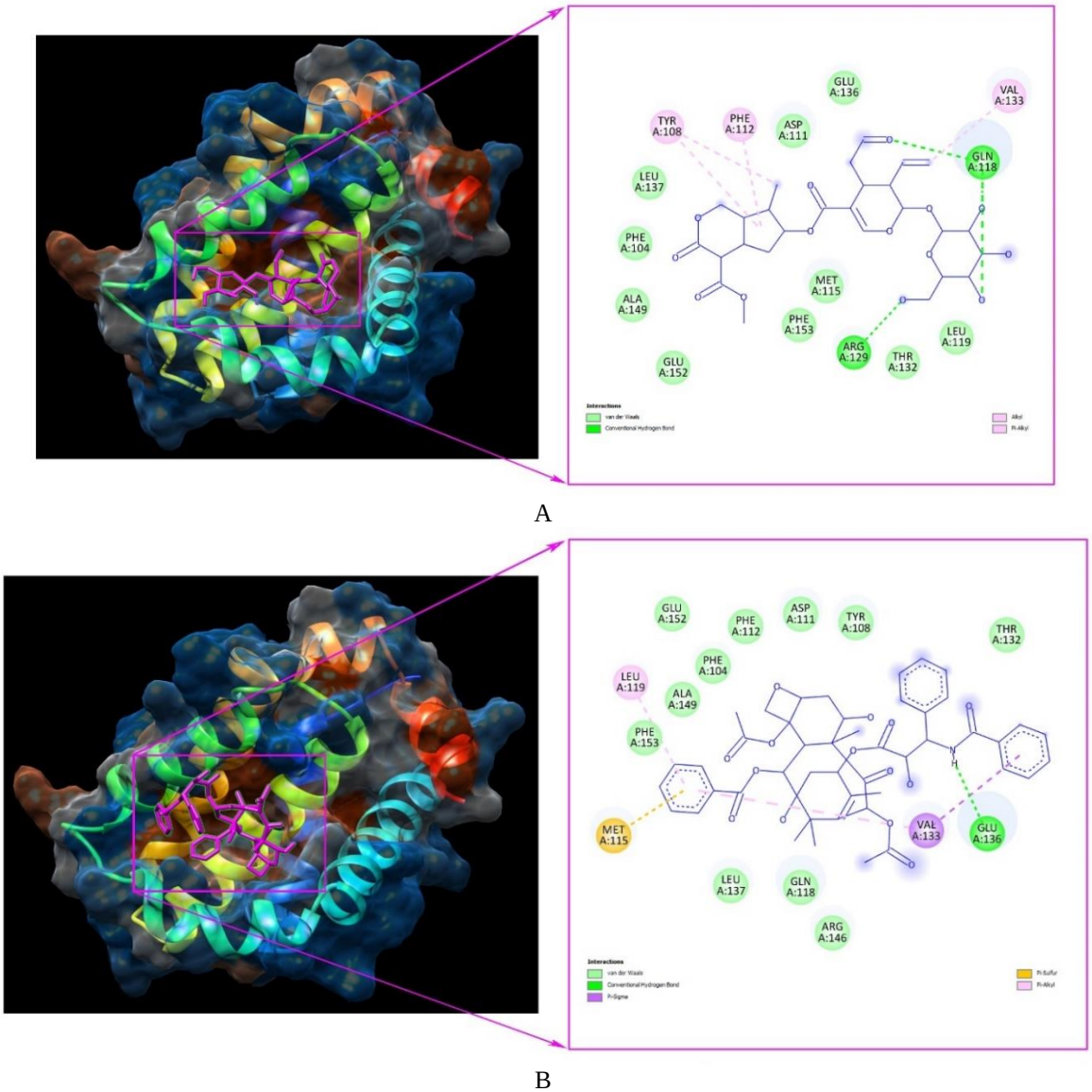


Figure 3. Molecular docking model and 2D interaction diagram of CPD6 (A) and Paclitaxel (B) with 6GL8 protein.

This open-access article is distributed under the terms of the Creative Commons Attribution Non Commercial 4.0 License (CC BY-NC 4.0).

Table 1. The interactions between the docked ligands and the protein 6GL8

Docked ligands	Binding energy (kcal/mol)	Hydrogen bond interaction	Van der Waals interaction	Hydrophobic interaction
CPD1	-6.67	-	Tyr108, Asp111, Gln118, Leu137, Phe150, Glu152, Phe153	Phe104, Phe112, Met115, Leu119, Val133, Ala149
CPD2	-6.59	-	Phe104, Tyr108, Asp111, Gln118, Leu119, Val133, Leu137	Phe112, Met115, Ala149, Phe153
CPD3	-6.68	Arg146	Phe104, Asp111, Phe112, Gln118, Leu119, Arg129, Thr132, Val133, Glu136, Leu137, Gly145, Ala149, Phe153	Tyr108, Met115
CPD4	-6.69	Tyr108, Arg146	Phe104, Asp111, Leu137, Asn143, Gly145, Ala149, Phe153	Phe112, Met115
CPD5	-6.99	Tyr108, Arg146	Arg107, Asp111, Met115, Gln118, Gly145	Phe104, Tyr108, Met112, Leu137, Ala149
CPD6	-7.68	Gln118, Arg129	Phe104, Asp111, Met115, Leu119, Thr132, Glu136, Leu137, Ala149, Glu152, Phe153	Tyr108, Phe112, Val133
CPD7	-6.51	Arg146	Asp111, Gln118, Ala149, Glu152	Phe104, Tyr108, Phe112, Met115, Val133, Leu137, Phe153
Paclitaxel	-6.18	Gln118, Glu136	Phe104, Tyr108, Asp111, Phe112, Thr132, Val133, Leu137, Arg146, Ala149, Glu152, Phe153	Leu119, Met115

The next strongest energy emerged for CPD5 (-6.99 kcal/mol), supported by 12 interactions composed of 2 hydrogen bonds (Tyr108, Arg146), 5 van der Waals contacts (Arg107, Asp111, Met115, Gln118, Gly145), and 5 hydrophobic contacts (Phe104, Tyr108, Met112, Leu137, Ala149), highlighting simultaneous polar anchoring (Tyr108/Arg146) and nonpolar packing around aromatic/aliphatic residues. Intermediate-energy ligands CPD4 (-6.69 kcal/mol) and CPD3 (-6.68 kcal/mol) exhibited distinct interaction architectures: CPD4 formed 11 interactions featuring 2 hydrogen bonds (Tyr108, Arg146), 7 van der Waals contacts (Phe104, Asp111, Leu137, Asn143, Gly145, Ala149, Phe153), and 2 hydrophobic contacts (Phe112, Met115), whereas CPD3 generated the largest contact count (16 interactions) with 1 hydrogen bond (Arg146), 13 van der Waals contacts (Phe104, Asp111, Phe112, Gln118, Leu119, Arg129, Thr132, Val133, Glu136, Leu137, Gly145, Ala149, Phe153), and 2 hydrophobic contacts (Tyr108, Met115), suggesting broad surface complementarity despite an energy comparable to CPD4. For the remaining ligands, CPD1 (-6.67 kcal/mol) achieved 13 interactions without hydrogen bonding, comprising 7 van der Waals contacts (Tyr108, Asp111, Gln118, Leu137, Phe150, Glu152, Phe153) and 6 hydrophobic contacts (Phe104, Phe112, Met115, Leu119, Val133, Ala149); CPD2 (-6.59 kcal/mol) displayed 11 interactions with 0 hydrogen bonds, 7 van der Waals contacts (Phe104, Tyr108, Asp111, Gln118, Leu119, Val133, Leu137), and 4 hydrophobic contacts (Phe112, Met115, Ala149, Phe153). CPD7 (-6.51 kcal/mol) maintained 12 interactions, including 1 hydrogen bond (Arg146), 4 van der Waals contacts (Asp111, Gln118, Ala149, Glu152), and 7 hydrophobic contacts (Phe104, Tyr108, Phe112, Met115, Val133, Leu137, Phe153), reflecting more substantial reliance on nonpolar enclosure than polar locking.

Relative to the reference, Paclitaxel showed 15 interactions with 2 hydrogen bonds (Gln118, Glu136), 11 van der Waals contacts (Phe104, Tyr108, Asp111, Phe112, Thr132, Val133, Leu137, Arg146, Ala149, Glu152, Phe153), and 2 hydrophobic contacts (Leu119, Met115). However, the binding energy (-6.18 kcal/mol) remained less favorable than the selected ligands (**Figure 3B**). Collectively, the dataset indicates that more negative binding energies coincided with cooperative contributions from directional hydrogen bonds (notably involving Gln118 and Arg129/Arg146 in higher-performing complexes), along with extensive short-range van der Waals complementarity and hydrophobic packing around aromatic and aliphatic pocket residues. Given its most favorable binding energy and multimodal

This open-access article is distributed under the terms of the Creative Commons Attribution Non Commercial 4.0 License (CC BY-NC 4.0).

interaction profile, CPD6 is prioritized as the primary candidate for subsequent molecular dynamics investigations. Accordingly, molecular dynamics simulations can assess whether the docked conformation remains stable over time and whether the principal hydrogen-bond and contact networks persist under protein flexibility and solvent effects.

3.2. Molecular Dynamics Simulations

Molecular dynamics simulations are powerful computational tools that reveal atomic-level details of physical, chemical, and biological processes, acting like a virtual microscope to show how atoms and molecules move and interact over time. This is crucial for understanding protein folding, drug binding, material properties, and complex reactions. By solving Newton's laws of motion for every atom, molecular dynamics simulations generate time-series data on atomic coordinates, revealing fluctuations, conformational changes, and dynamics not easily seen experimentally, bridging the gap between theory and observation in fields from physics and chemistry to materials science and biomedicine [28]. Combining molecular docking with molecular dynamics simulations creates a robust drug discovery strategy, using docking for rapid screening of large compound libraries to find potential binders, and then using the more computationally intensive molecular dynamics to refine poses, account for protein flexibility, analyze dynamic interactions, and accurately calculate binding energies, leading to more reliable identification of stable, effective drug candidates [29]. Therefore, the evaluation systematically examined RMSD, RMSF, Rg, Hbonds, and SASA to assess the stability, flexibility, and solvent exposure of the CPD6-6GL8 and Paclitaxel-6GL8 complexes throughout the simulation. Consequently, the total and potential energy values for the CPD6-6GL8 complex were -227,590 kJ/mol and -282,633 kJ/mol, respectively. For the Paclitaxel-6GL8 complex, the total and potential energy values were -225,831 kJ/mol and -280,908 kJ/mol, respectively. The simulation system remained in equilibrium at 300 K.

In molecular dynamics simulations, RMSD quantifies how much a molecule's structure changes over time or differs from a reference by measuring the average distance between atoms after optimal alignment. Researchers commonly use RMSD vs. time plots to assess simulation stability and conformational changes, indicating whether the system has settled or undergone significant structural shifts. A stable system exhibits low, plateaued RMSD, while large fluctuations or increasing RMSD indicate instability or unfolding. Lower RMSD generally signifies less deviation and greater stability [30]. Over the 100 ns trajectory, the CPD6-6GL8 complex showed a rapid accommodation phase, followed by sustained confinement of RMSD values, remaining approximately within 0.16-0.22 nm, with an average near 0.19 nm. A comparable pattern characterized the Paclitaxel-6GL8 complex, whose RMSD fluctuated within approximately 0.16-0.23 nm, with a center of 0.19 nm (**Figure 4A**). The close overlap between profiles, together with the absence of progressive divergence, suggests that the reference conformation is preserved for both assemblies under dynamic conditions. In contrast, the CPD6-6GL8 trajectory exhibited a marginally lower upper excursion relative to the Paclitaxel-6GL8 complex.

In molecular dynamics simulations, RMSF measures the flexibility and movement of individual atoms or residues over a simulation, showing how much they deviate from their average positions. A high RMSF indicates a region of a protein that is very flexible, dynamic, and less structurally stable, while a low RMSF signifies a rigid, stable part of the protein that moves very little from its average position [31]. Within the Gly7-Gly203 interval (**Figure 4B**), the CPD6-6GL8 complex exhibited RMSF values of approximately 0.03-0.15 nm with a mean near 0.04 nm, whereas the Paclitaxel-6GL8 complex spanned approximately 0.03-0.2 nm with a mean near 0.04 nm. Despite these maxima, fluctuations across most residues in this segment remained predominantly low, clustering around 0.03-0.06 nm, consistent with constrained motions and preservation of local structural integrity after the initial N-terminal flexibility. Overall, the two profiles overlapped closely throughout Gly7-Gly203, while the higher early-residue excursion observed for Paclitaxel relative to CPD6 suggests greater terminal mobility under the reference-ligand condition within this selected region.

The radius of gyration (Rg) describes the mass-weighted spatial distribution of atoms around the

This open-access article is distributed under the terms of the Creative Commons Attribution Non Commercial 4.0 License (CC BY-NC 4.0).

molecular center of mass. It is routinely used to evaluate the global compactness of molecules during molecular dynamics. Lower Rg values generally correspond to a more compact fold, whereas higher values indicate a more expanded conformation. As shown in **Figure 4C**, both CPD6-6GL8 and Paclitaxel-6GL8 trajectories underwent a brief early relaxation from approximately 1.47 nm toward the 1.44 nm region, followed by sustained fluctuations within a narrow band across the 100 ns simulation. The CPD6-6GL8 complex maintained Rg values of approximately 1.42-1.47 nm (mean near 1.44 nm), while the Paclitaxel-6GL8 complex remained approximately within 1.43-1.46 nm (mean close to 1.44 nm). Overall, Rg's persistent confinement around 1.44 nm supports the preservation of a stable, compact global architecture for 6GL8 in both bound states, with a slightly lower central tendency observed for the CPD6 complex.

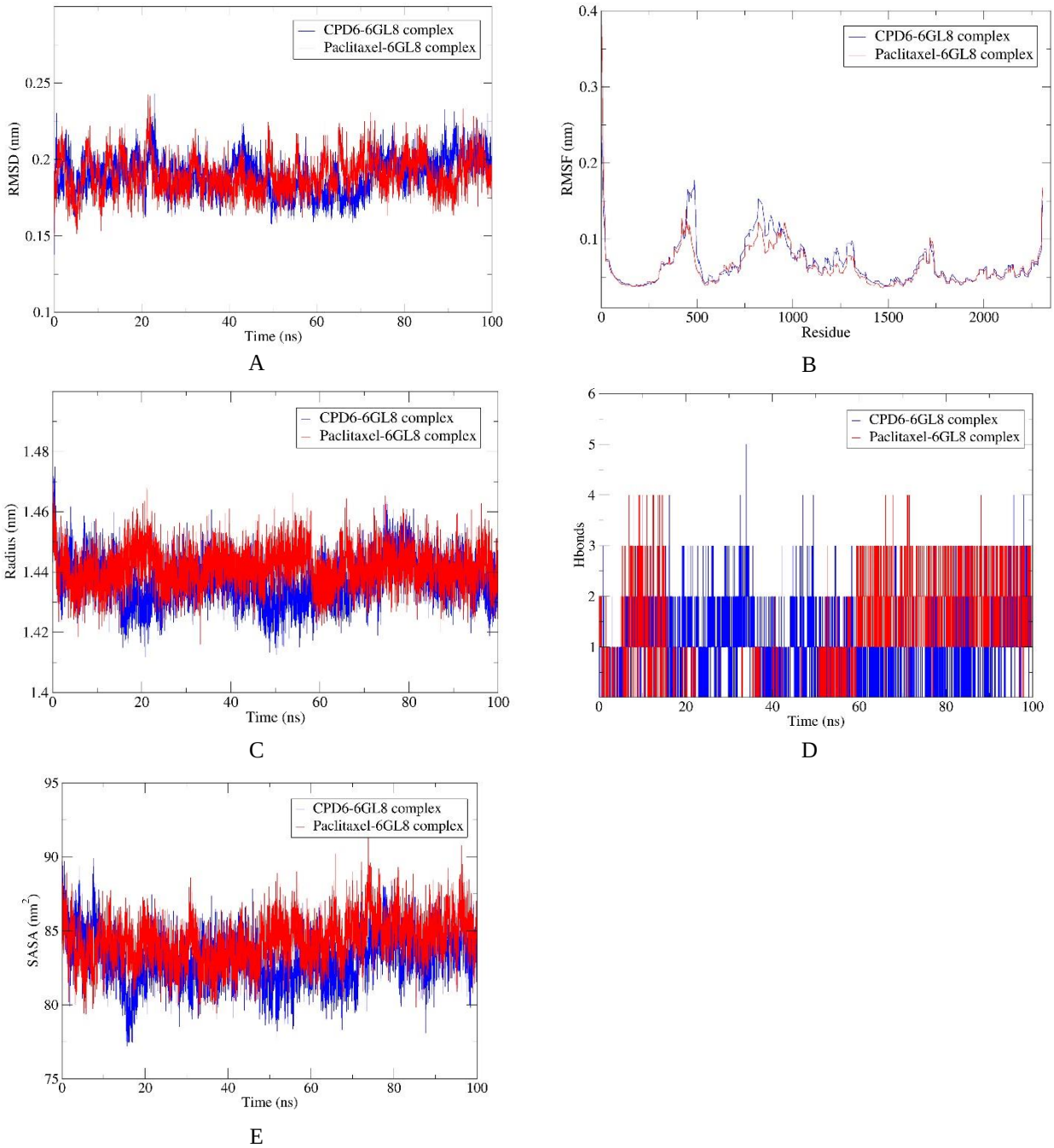


Figure 4. Results of MD simulation for the bindings of CPD6 (blue) and Paclitaxel (red) with 6GL8 protein. (A) RMSD, (B) RMSF, (C) Rg, (D) Hbonds, (E) SASA.

This open-access article is distributed under the terms of the Creative Commons Attribution Non Commercial 4.0 License (CC BY-NC 4.0).

In drug discovery and molecular docking studies, hydrogen bonds often mediate specific interactions between proteins and ligands/small drug molecules. These interactions contribute significantly to binding affinity and specificity. An increased number of H-bonds in a molecular dynamics simulation generally signifies stronger, more stable intermolecular interactions, leading to greater complex stability, slower diffusion, higher melting points, and better mechanical properties in systems like protein-ligand complexes, polymer blends, or crystals, as these H-bonds contribute significantly to overall binding energy and structural integrity [32]. Over the 100 ns simulation (**Figure 4D**), the CPD6-6GL8 complex exhibited hydrogen-bond numbers spanning 0-5, with the trajectory most frequently occupying approximately 1-2 bonds and showing intermittent excursions to higher counts (≥3), including a brief maximum near 5. In contrast, the Paclitaxel-6GL8 complex fluctuated between 0 and 4 hydrogen bonds, with recurrent occupancy of 2-3 bonds during extended intervals, particularly in the late stage of the simulation, alongside occasional peaks reaching 4. Overall, the hydrogen-bond profile indicates that Paclitaxel maintained a more continuous polar-contact regime across substantial portions of the trajectory, whereas CPD6 displayed a more discontinuous hydrogen-bond pattern punctuated by short-lived high-count events, consistent with stabilization that may rely more heavily on non-hydrogen-bond interactions in addition to transient polar anchoring.

The SASA measures the extent to which a molecule is exposed to solvent, calculated by rolling a probe sphere over its surface. This is crucial for understanding protein folding, stability, ligand binding, and conformational changes during simulations, thereby revealing protein dynamics and interactions. As shown in **Figure 4E**, the SASA profiles for both complexes fluctuated within a confined interval over 100 ns, without sustained upward or downward drift, indicating largely preserved solvent exposure under bound conditions. The CPD6-6GL8 complex exhibited SASA values of approximately 77-90 nm^2, with a trajectory-average near 82.7 nm^2, whereas the Paclitaxel-6GL8 complex remained approximately within 81-90 nm^2 and centered around 84.2 nm^2. A modest downward shift in the CPD6 trace relative to Paclitaxel suggests reduced solvent exposure and slightly greater compactness for the CPD6-bound state. At the same time, the comparable oscillatory behavior in both systems supports a stable global architecture throughout the simulation window.

Overall, the integrated molecular dynamics readouts indicate sustained structural integrity for the CPD6-6GL8 complex and a stability profile comparable to the reference ligand, while suggesting a slightly more compact and less solvent-exposed bound state that supports persistent accommodation within the 6GL8 binding pocket.

3.3. Free binding energy (MMGBSA) analysis

Molecular Mechanics with Generalized Born Surface Area (MMGBSA) is a powerful computational method in drug discovery, used to quickly estimate how strongly potential ligands bind to target proteins by calculating binding free energies from molecular dynamics simulations, breaking down interactions (electrostatic, van der Waals, solvation) to identify key binding drivers and prioritize drug candidates for new therapies against diseases. This approach can be complemented by techniques such as virtual screening and molecular dynamics simulations [33]. Binding free energies for the CPD6-6GL8 and Paclitaxel-6GL8 complexes were evaluated using the MM/GBSA framework, where the binding term is defined as $\Delta G_bind = G_complex - (G_receptor + G_ligand)$. In an equivalent thermodynamic form, ΔG_bind may be written as $\Delta H - T\Delta S$; however, omission of the entropic component yields an enthalpy-dominated descriptor that remains appropriate for comparative ranking between closely related systems. The resulting mean energies and their dispersions describe the balance between gas-phase interactions ($\Delta G_GAS = \Delta VDWAALS + \Delta EEL$) and solvation effects ($\Delta G_SOLV = \Delta EGB + \Delta ESURF$), thereby enabling mechanistic interpretation through energy decomposition.

As detailed in **Table 2**, both complexes exhibit favorable association, reflected by negative ΔTOTAL values: -27.28 ± 4.80 kcal/mol for CPD6-6GL8 and -30.47 ± 7.30 kcal/mol for Paclitaxel-6GL8, with Paclitaxel showing the more advantageous mean by 3.19 kcal/mol. Gas-phase contributions slightly favor CPD6

This open-access article is distributed under the terms of the Creative Commons Attribution Non Commercial 4.0 License (CC BY-NC 4.0).

(ΔG_GAS = -59.87 ± 10.78 kcal/mol) over Paclitaxel (-57.06 ± 14.27 kcal/mol), driven primarily by stronger electrostatics for CPD6 (ΔEEL = -19.27 ± 8.98 kcal/mol versus -14.58 ± 10.50 kcal/mol). In contrast, van der Waals interactions favor Paclitaxel (ΔVDWAALS = -42.48 ± 6.30 kcal/mol versus -40.61 ± 5.09 kcal/mol). In comparison, solvation penalties are substantially lower for Paclitaxel (ΔG_SOLV = 26.59 ± 8.16 kcal/mol) than for CPD6 (32.59 ± 8.36 kcal/mol), mainly attributable to a reduced polar solvation term (ΔEGB = 32.31 ± 8.78 kcal/mol versus 38.28 ± 8.56 kcal/mol), while nonpolar solvation remains nearly identical (ΔESURF -5.7 kcal/mol for both). Paclitaxel binding shows greater variability, as indicated by the higher standard deviation in ΔTOTAL (7.30 vs. 4.80 kcal/mol), consistent with broader temporal dispersion of interaction energetics despite the more favorable mean affinity estimate. Although Paclitaxel shows a marginally more favorable mean ΔTOTAL, the 3.19 kcal/mol difference falls within the overlapping standard deviations of both estimates (±4.80 and ±7.30 kcal/mol) and does not establish a definitive thermodynamic hierarchy. The selection of CPD6 for emphasis therefore rests on a convergence of complementary indicators, the foremost docking rank among the screened iridoids, sustained conformational stability, an absent hepatotoxicity alert, and a reactive frontier-orbital profile, rather than on binding free energy alone.

3.4. ADMET prediction analysis

In silico ADMET profiling was performed to elucidate the predicted pharmacokinetic behavior and safety-relevant alerts of CPD6 in comparison with the reference agent, Paclitaxel, with principal descriptors organized across absorption, distribution, metabolism, excretion, and toxicity categories. This comparative output provides a unified basis for anticipating liabilities and prioritizing candidates in computational screening for hepatocellular carcinoma-relevant inhibitors. ADMET-related descriptors predicted for CPD6 and the reference compound Paclitaxel are detailed in **Table 3**.

Across absorption-related descriptors, both ligands display identical predicted aqueous solubility (water solubility: -3.518 log mol/L for CPD6 and -3.518 log mol/L for Paclitaxel), indicating similarly limited dissolution under the applied model. Permeability metrics, however, diverge substantially. CPD6 exhibits markedly reduced predicted human intestinal absorption (38.048%) relative to Paclitaxel (100%), together with a lower Caco-2 permeability (-0.372 versus 0.623 log Papp in 10^{-6} cm/s). Dermal permeation estimates remain comparable, with skin permeability values of -2.738 (CPD6) and -2.735 (Paclitaxel). Transporter-related annotations indicate shared involvement with P-glycoprotein, as both compounds are predicted to be substrates and inhibitors of P-glycoprotein I; additional differentiation arises from P-glycoprotein II inhibition, which is expected for Paclitaxel but not for CPD6.

Distribution parameters further distinguish systemic disposition tendencies. The predicted steady-state volume of distribution is lower for CPD6 (VDss = 0.222 log L/kg) than for Paclitaxel (1.458 log L/kg), suggesting more constrained tissue distribution for CPD6 within this framework. Plasma protein binding predictions also separate the profiles: CPD6 retains a measurable unbound fraction (Fu = 0.312), whereas Paclitaxel is reported with Fu = 0, consistent with near-complete binding in the model output. Central exposure is predicted to be limited for both candidates, as indicated by strongly negative BBB permeability (logBB = -2.257 for CPD6 and -1.731 for Paclitaxel) and CNS permeability (logPS = -4.691 for CPD6 and -3.85 for Paclitaxel), with Paclitaxel showing less restrictive values than CPD6 for both indices.

Table 2. Free energy of binding obtained using MMGBSA calculations.

Energy Component	Average (kcal/mol)		Standard Deviation	
	CPD6-6GL8	Paclitaxel-6GL8	CPD6-6GL8	Paclitaxel-6GL8
ΔVDWAALS	-40.61	-42.48	5.09	6.30
ΔEEL	-19.27	-14.58	8.98	10.50
ΔEGB	38.28	32.31	8.56	8.78
ΔESURF	-5.69	-5.71	0.65	0.93
ΔGGAS	-59.87	-57.06	10.78	14.27
ΔGSOLV	32.59	26.59	8.36	8.16
ΔTOTAL	-27.28	-30.47	4.80	7.30

This open-access article is distributed under the terms of the Creative Commons Attribution Non Commercial 4.0 License (CC BY-NC 4.0).

Table 3. Predicted ADMET properties of CPD6 and Paclitaxel.

ADMET properties	Unit	CPD6	Paclitaxel
Water Solubility	(Log mol/L)	-3.518	-3.158
Caco2 permeability	(Log Papp in 10^{-6} cm/s)	-0.372	0.623
Intestinal absorption (Human)	(% Absorbed)	38.048	100
Skin permeability	(Log Kp)	-2.738	-2.735
P-glycoprotein substrate	Yes/No	Yes	Yes
P-glycoprotein I inhibitor	Yes/No	Yes	Yes
P-glycoprotein II inhibitor	Yes/No	No	Yes
VDss	(Log L/kg)	0.222	1.458
Fraction unbound (human)	(Fu)	0.312	0
BBB permeability	(Log BB)	-2.257	-1.731
CNS permeability	(Log PS)	-4.691	-3.95
CYP2D6 substrate	Yes/No	No	No
CYP3A4 substrate	Yes/No	No	Yes
CYP1A2 inhibitor	Yes/No	No	No
CYP2C19 inhibitor	Yes/No	No	No
CYP2C9 inhibitor	Yes/No	No	No
CYP2D6 inhibitor	Yes/No	No	No
CYP3A4 inhibitor	Yes/No	No	Yes
Total clearance	(Log ml/min/kg)	1.015	-0.36
Renal OCT2 substrate	Yes/No	No	No
AMES toxicity	Yes/No	No	No
Max. tolerated dose (human)	(Log mg/kg/day)	-0.176	0.199
hERG I inhibitor	Yes/No	No	No
hERG II inhibitor	Yes/No	Yes	Yes
Oral rat acute toxicity (LD50)	(mol/kg)	4.256	2.776
Oral rat chronic toxicity (LOAEL)	(Log mg/kg_bw/day)	3.855	3.393
Hepatotoxicity	Yes/No	No	Yes
Skin sensation	Yes/No	No	No
Tetrahymena pyriformis toxicity	(Log ug/L)	0.285	0.285
Minnow toxicity	(Log mM)	7.076	2.988

Metabolic handling predictions reveal distinct CYP-associated interaction potential. Neither ligand is categorized as a CYP2D6 substrate. CPD6 is negative for CYP3A4 substrate status, whereas Paclitaxel is annotated as both a CYP3A4 substrate and a CYP3A4 inhibitor; however, CPD6 remains negative for CYP3A4 inhibition. No inhibitory flags are assigned to either compound for CYP1A2, CYP2C19, CYP2C9, or CYP2D6, indicating an absence of predicted inhibition across these isoforms in the present output.

Excretion-related estimates indicate higher predicted elimination capacity for CPD6 (1.015 log ml/min/kg) relative to Paclitaxel (-0.36 log ml/min/kg). The renal OCT2 substrate status is negative for both molecules, indicating no OCT2-associated renal transport designation under the same prediction settings.

Toxicity endpoints present a mixed pattern of liabilities. Both compounds are predicted to be AMES-negative and hERG I inhibitor-negative, whereas hERG II inhibition is flagged for both CPD6 and Paclitaxel. A notable divergence is observed for hepatotoxicity, which is predicted to be negative for CPD6 and positive for Paclitaxel; skin sensitization is expected to be negative for both. Quantitative tolerance/toxicity indices further differentiate the candidates: the maximum tolerated dose is -0.176 log mg/kg/day for CPD6 and 0.199 for Paclitaxel; oral rat acute toxicity (LD50) is 4.256 mol/kg for CPD6 and 2.776 mol/kg for Paclitaxel; oral rat chronic toxicity (LOAEL) is 3.855 log mg/kg_bw/day for CPD6 and 3.393 for Paclitaxel. Ecotoxicity-associated descriptors show identical *Tetrahymena pyriformis* toxicity (0.285 log µg/L for both), while minnow toxicity differs markedly (7.076 log mM for CPD6 vs 2.988 log mM for Paclitaxel).

Collectively, the ADMET output indicates that CPD6 shares similarly poor predicted solubility with Paclitaxel but shows substantially reduced intestinal absorption and Caco-2 permeability, along with lower predicted

This open-access article is distributed under the terms of the Creative Commons Attribution Non Commercial 4.0 License (CC BY-NC 4.0).

distribution (VDss) and more restricted BBB/CNS penetration. In contrast, CPD6 exhibits a nonzero unbound fraction and higher predicted total clearance, but lacks the CYP3A4 substrate/inhibitor annotations typically assigned to Paclitaxel. Safety-related predictions highlight a hepatotoxicity alert for Paclitaxel but not for CPD6, while hERG II inhibition remains a shared concern. These distinctions support differential prioritization for subsequent validation within a computational modeling workflow targeting iridoid-derived candidates as potential inhibitors relevant to hepatocellular carcinoma.

3.5. Quantum chemistry computation using the DFT method

In modern drug discovery, Density Functional Theory (DFT) is crucial for accurately modeling electronic structures, predicting reactivity, understanding drug-target binding (like H-bonds, π-stacking), guiding molecular design for better stability/efficacy, and generating features for AI/ML models, bridging quantum-level details with macroscopic drug behavior for faster, more informed development. It provides chemical accuracy beyond classical methods, revealing mechanisms like metabolic hotspots and transition states vital for designing effective and safe therapeutics [34]. We applied DFT-based quantum chemical analysis after the classical modeling stage to characterize the electronic structure and infer reactivity-related tendencies of CPD6 relative to the reference Paclitaxel. The calculated descriptors comprised EHOMO (eV), ELUMO (eV), ΔE (eV), μ (eV), χ (eV), η (eV), σ (eV-1), and ω (eV), which collectively describe frontier-orbital energetics, resistance to charge redistribution, and electrophilic character. Within this framework, EHOMO (eV) reflects the propensity for electron donation, whereas ELUMO (eV) indicates the capacity for electron acceptance; ΔE (eV), defined as the difference between ELUMO (eV) and EHOMO (eV), provides an index of electronic stability versus chemical responsiveness. DFT calculations for CPD6 and the reference compound, Paclitaxel, are detailed in **Table 4**.

For CPD6, EHOMO (eV) equals -8.2912, exceeding the corresponding value for Paclitaxel (-8.6942), a relationship consistent with relatively more straightforward electron donation for CPD6 under the computed conditions. A pronounced separation appears in ELUMO (eV), where CPD6 shows -4.4907 while Paclitaxel displays 2.1568, indicating a markedly lower-lying acceptor orbital for CPD6. Consequently, CPD6's ΔE (eV) is 3.8005, substantially smaller than Paclitaxel's 10.851, supporting greater electronic polarizability and potentially higher chemical responsiveness for CPD6. In contrast, the wider gap in Paclitaxel aligns with increased frontier-orbital stability (**Figure 5**).

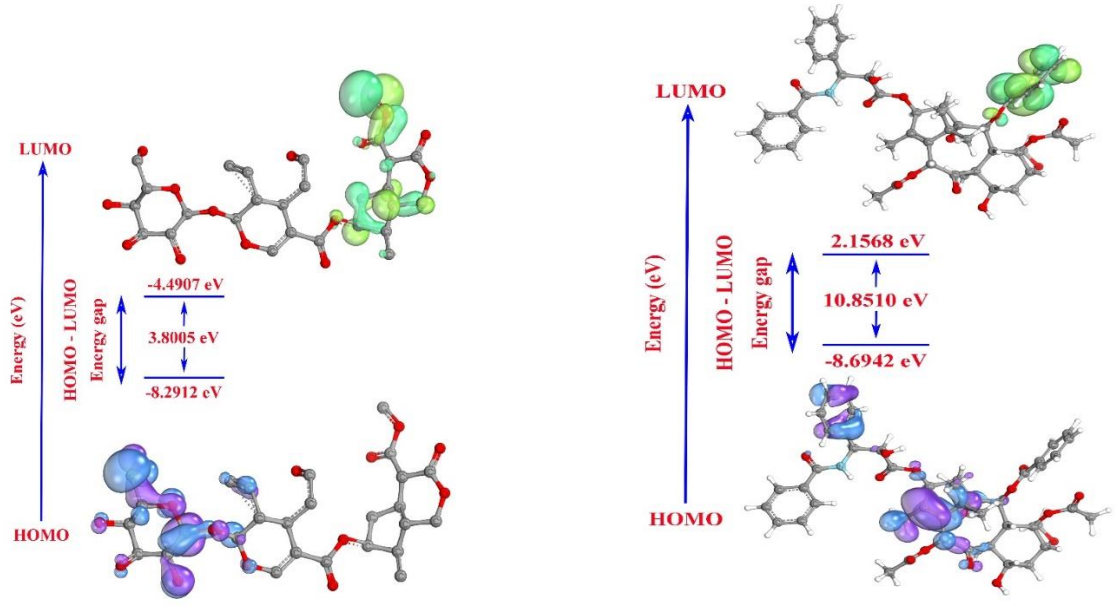


Figure 5. HOMO and LUMO surface diagrams of CPD6 (A) and Paclitaxel (B).

This open-access article is distributed under the terms of the Creative Commons Attribution Non Commercial 4.0 License (CC BY-NC 4.0).

Table 4. Quantum descriptors of CPD6 and Paclitaxel.

Molecule	EHOMO (eV)	ELUMO (eV)	ΔE (eV)	μ (eV)	χ (eV)	η (eV)	σ (eV^{-1})	ω (eV)
CPD6	-8.2912	-4.4907	3.8005	-6.3910	6.3910	1.9003	0.5262	10.7471
Paclitaxel	-8.6942	2.1568	10.8510	-3.2687	3.2687	5.4255	0.1843	0.9846

EHOMO (eV): highest occupied molecular orbitals; **ELUMO (eV)**: lowest unoccupied molecular orbitals; **ΔE (eV)**: energy gap; **μ (eV)**: chemical potential; **χ (eV)**: electronegativity; **η (eV)**: hardness; **σ (eV^{-1})**: softness; **ω (eV)**: electrophilicity index.

Global reactivity descriptors further reinforce this contrast. The χ (eV) value of CPD6 (6.3910) exceeds that of Paclitaxel (3.2687), indicating a stronger electron-attracting character for CPD6 in the present calculation. Consistently, the μ (eV) values mirror the expected inverse relationship with χ (eV), with CPD6 presenting a more negative chemical potential (-6.3910) than Paclitaxel (-3.2687), implying a comparatively stronger thermodynamic tendency toward electron uptake. Resistance to electronic deformation, quantified by η (eV), is lower for CPD6 (1.9003) than for Paclitaxel (5.4255), and the corresponding σ (eV-1) values follow the reciprocal trend, with CPD6 exhibiting higher softness (0.5262) than Paclitaxel (0.1843). Finally, ω (eV), which captures electrophilic strength, is markedly elevated for CPD6 (10.7471) relative to Paclitaxel (0.9846), indicating a substantially stronger electrophilicity index for CPD6 in this DFT dataset.

4. Conclusion

This study assessed iridoid-derived candidates from *P. hookeri* as potential inhibitors of the Bcl-2 protein (PDB ID: 6GL8) by integrating docking, 100-ns molecular dynamics simulations, MMGBSA calculations, ADMET predictions, and DFT descriptors. Docking prioritized CPD6 as the best-performing ligand, whose binding affinity surpassed that of the reference agent paclitaxel and relied on directional hydrogen bonding with Gln118 and Arg129. During 100 ns simulations, CPD6-6GL8 preserved stable structural behavior comparable to the paclitaxel-bound system, while adopting a marginally more compact and less solvent-exposed conformation. MMGBSA calculations corroborated a thermodynamically favorable association for both complexes, with CPD6 binding governed predominantly by gas-phase electrostatic stabilization but attenuated by a higher solvation penalty. ADMET predictions indicated comparable aqueous solubility but reduced intestinal absorption and higher predicted clearance for CPD6 than for Paclitaxel.

Additionally, a hepatotoxicity alert was noted for Paclitaxel but not for CPD6. DFT calculations further differentiated the electronic behavior of the two compounds, with CPD6 displaying a narrower HOMO-LUMO gap and a higher electrophilicity index, consistent with greater chemical reactivity. Overall, the combined results support CPD6 as a promising lead scaffold for 6GL8 inhibition, while absorption-related limitations indicate the need for subsequent optimization and experimental validation.

Conflict of interest

No funding was received for conducting this research. This work does not contain any studies involving human and animal subjects.

Authors Orcid numbers:

Hung Duc Nguyen: 0000-0002-5764-1242

Using artificial intelligence chatbots

There was no use of artificial intelligence in the making of this article.

References

1. Bray F, Laversanne M, Sung H, Ferlay J, Siegel RL, Soerjomataram I, Jemal A. Global cancer statistics 2022: GLOBOCAN estimates of incidence and mortality worldwide for 36 cancers in 185 countries. *CA. Cancer J. Clin.* (2024) 74 (3):229-263.

This open-access article is distributed under the terms of the Creative Commons Attribution Non Commercial 4.0 License (CC BY-NC 4.0).

2. Chidambaranathan-Reghupaty S, Fisher PB, Sarkar D. Hepatocellular carcinoma (HCC): Epidemiology, etiology and molecular classification. Sarkar D, Fisher PB (Eds.) In: Advances in Cancer Research, Academic Press, Oxford (2021) 1-61.
3. Vogler M, Braun Y, Smith VM, Westhoff MA, Pereira RS, Pieper NM, Anders M et al. The BCL2 family: from apoptosis mechanisms to new advances in targeted therapy. Signal Transduct. Target. Ther. (2025) 10 (1):91.
4. Correia C, Lee SH, Meng XW, Vincelette ND, Knorr KLB, Ding H, Nowakowski GS et al. Emerging understanding of Bcl-2 biology: Implications for neoplastic progression and treatment. Biochim. Biophys. Acta - Mol. Cell Res. (2015) 1853 (7):1658-1671.
5. Warren CFA, Wong-Brown MW, Bowden NA. BCL-2 family isoforms in apoptosis and cancer. Cell Death Dis. (2019) 10 (3):177.
6. Shah U, Shah R, Acharya S, Acharya N. Novel anticancer agents from plant sources. Chin. J. Nat. Med. (2013) 11 (1):16-23.
7. Seca AML, Pinto DCGA. Plant secondary metabolites as anticancer agents: Successes in clinical trials and therapeutic application. Int. J. Mol. Sci. (2018) 19 (1):263.
8. Cao Q, Du X, Liu A, Li Q, Luo Q, Chen Y, Wang R, Meng L. Iridoids in gardenia fruit: key components in liver disease therapy. Front. Nutr. (2025) 12:1667863.
9. Ndongwe T, Witika BA, Mncwangi NP, Poka MS, Skosana PP, Demana PH, Summers B et al. Iridoid derivatives as anticancer agents: An updated review from 1970-2022. Cancers (2023) 15 (3):770.
10. Kim CW, Choi KC. Potential roles of iridoid glycosides and their underlying mechanisms against diverse cancer growth and metastasis: Do they have an inhibitory effect on cancer progression? Nutrients (2021) 13 (9):2974.
11. Gan Z, Jiang J, Tao H, Luo S, Meng X, Yu J, Zhang Y et al. Traditional uses, phytochemistry, pharmacology, and toxicology of Pterocephalus hookeri (C. B. Clarke) Höeck: a review. RSC Adv. (2021) 11 (46):28761-28774.
12. Dong Z, Xiong Y, Zhang R, Qiu Y, Meng F, Liao Z, Lan X et al. Ptehosides A-I: Nine undescribed iridoids with in vitro cytotoxicity from the whole plant of Pterocephalus hookeri (C.B. Clarke) Höeck. Phytochemistry (2024) 223:114144.
13. Murray JB, Davidson J, Chen I, Davis B, Dokurno P, Graham CJ, Harris R et al. Establishing drug discovery and identification of hit series for the anti-apoptotic proteins, Bcl-2 and Mcl-1. ACS Omega (2019) 4 (5):8892-8906.
14. Nguyen HD. DFT and molecular modelling reveal the mechanism of action of selected alkaloids as anti-colorectal cancer agents targeting topoisomerase II. Not. Sci. Biol. (2025) 17 (3):12642.
15. Van Der Spoel D, Lindahl E, Hess B, Groenhof G, Mark AE, Berendsen HJ. GROMACS: Fast, flexible, and free. J. Comput. Chem. (2005) 26 (16):1701-1718.
16. Guex N, Peitsch MC. SWISS-MODEL and the Swiss-Pdb Viewer: An environment for comparative protein modeling. Electrophoresis (1997) 18 (15):2714-2723.
17. Zoete V, Cuendet MA, Grosdidier A, Michielin O. SwissParam: A fast force field generation tool for small organic molecules. J. Comput. Chem. (2011) 32 (11):2359-2368.
18. Pettersen EF, Goddard TD, Huang CC, Couch GS, Greenblatt DM, Meng EC, Ferrin TE. UCSF Chimera-A visualization system for exploratory research and analysis. J. Comput. Chem. (2004) 25 (13):1605-1612.
19. Nguyen HD. Unveiling the anti-apoptotic mechanism of magnolialide as a colorectal cancer inhibitor via molecular modeling, ADMET, and MMGBSA analysis. Phys. Chem. Res. (2025) 13 (4):783-796.
20. Neese F. Software update: The ORCA program system-version 6.0. WIREs Comput. Mol. Sci. (2025) 15 (2):e70019.
21. Knizia G, Klein JE. Electron flow in reaction mechanisms-revealed from first principles. Angew. Chemie Int. Ed. (2015) 54 (18):5518-5522.
22. Hanwell MD, Curtis DE, Lonie DC, Vandermeersch T, Zurek E, Hutchison GR. Avogadro: an advanced semantic chemical editor, visualization, and analysis platform. J. Cheminform. (2012) 4 (1):17.
23. Luo J, Xue ZQ, Liu WM, Wu JL, Yang ZQ. Koopmans' theorem for large molecular systems within density functional theory. J. Phys. Chem. A (2006) 110 (43):12005-12009.
24. Das R, Vigneresse JL, Chattaraj PK. Chemical reactivity through structure-stability landscape. Int. J. Quantum Chem. (2014) 114 (21):1421-1429.
25. Pinzi L, Rastelli G. Molecular docking: Shifting paradigms in drug discovery. Int. J. Mol. Sci. (2019) 20 (18):4331.
26. Patil R, Das S, Stanley A, Yadav L, Sudhakar A, Varma AK. Optimized hydrophobic interactions and hydrogen bonding at the target-ligand interface leads the pathways of drug-designing. PLoS One (2010) 5 (8):e12029.
27. Bitencourt-Ferreira G, Veit-Acosta M, de Azevedo WF. Van der Waals potential in protein complexes. de Azevedo Jr WF (Ed.) In: Docking Screens for Drug Discovery, Springer, New York (2019) 79-91.

This open-access article is distributed under the terms of the Creative Commons Attribution Non Commercial 4.0 License (CC BY-NC 4.0).

28. Padhi AK, Janežič M, Zhang KYJ. Molecular dynamics simulations: Principles, methods, and applications in protein conformational dynamics. Tripathi T and Dubey VK (Eds.) In: Advances in Protein Molecular and Structural Biology Methods, Academic Press, Oxford (2022) 439-54.
29. Alonso H, Bliznyuk AA, Gready JE. Combining docking and molecular dynamic simulations in drug design. Med. Res. Rev. (2006) 26 (5):531-568.
30. Sargsyan K, Grauffel C, Lim C. How molecular size impacts rmsd applications in molecular dynamics simulations. J. Chem. Theory Comput. (2017) 13 (4):1518-1524.
31. Ghahremanian S, Rashidi MM, Raeisi K, Toghraie D. Molecular dynamics simulation approach for discovering potential inhibitors against SARS-CoV-2: A structural review. J. Mol. Liq. (2022) 354 :118901.
32. Dhar M, Tiwari RK. Molecular dynamics simulation insights into hydrogen bonding-mediated conformational changes topoisomerase-IB. Macromol. Symp. (2024) 413 (5):2400036.
33. Adediwura VA, Koirala K, Do HN, Wang J, Miao Y. Understanding the impact of binding free energy and kinetics calculations in modern drug discovery. Expert Opin. Drug Discov. (2024) 19 (6):671-682.
34. Niazi SK. Quantum mechanics in drug discovery: A comprehensive review of methods, applications, and future directions. *Int. J. Mol. Sci.* (2025) 26 (13):6325.

This open-access article is distributed under the terms of the Creative Commons Attribution Non Commercial 4.0 License (CC BY-NC 4.0).